

# Wide parameter-space O3 search for continuous gravitational waves from unknown neutron stars in binary systems

P. B. COVAS,<sup>1,2</sup> M. A. PAPA,<sup>1</sup> AND R. PRIX<sup>1</sup>

<sup>1</sup>*Max Planck Institute for Gravitational Physics (Albert Einstein Institute) and Leibniz Universität Hannover, D-30167 Hannover, Germany*

<sup>2</sup>*Departament de Física, Universitat de les Illes Balears, IAC3, Carretera Valldemossa km 7.5, E-07122 Palma, Spain*

## ABSTRACT

Continuous gravitational waves, i.e., persistent and nearly-monochromatic signals emitted by asymmetric spinning neutron stars, remain elusive. Searches for these signals from unknown *binary* systems are the most computationally challenging, but they are essential, given that binary accretion provides a natural mechanism for creating the required asymmetry, and around half of the known pulsars rotating above 25 Hz are part of a binary system. Here we report on a search of a large uncharted parameter-space region: for the first time we cover gravitational-wave frequencies above 520 Hz (from 50 to 1000 Hz), and, for the first time with advanced detectors, orbital periods lower than 3 days are explored. No signal is detected, and we set the most stringent constraints to date on the amplitude of signals of this kind. Our results exclude with 95% confidence neutron stars within 100 pc and rotating faster than  $\sim 495$  Hz from having ellipticities above  $5.2 \times 10^{-8}$ . Within the same distance our results also exclude r-mode amplitudes above  $1.5 \times 10^{-6}$  for stars rotating faster than  $\sim 740$  Hz.

*Keywords:* Gravitational waves (678) — Neutron stars(1108)

## 1. INTRODUCTION

Continuous gravitational waves (CWs), which are yet to be detected, may be sourced by rotating neutron stars with a time-varying quadrupole (Riles 2023). This quadrupole can be generated by a mass asymmetry or an unstable oscillation mode like the r-mode (Jones & Riles 2025).

Searches for these signals can be categorized based on the type of prior knowledge of the source. Targeted searches focus on known pulsars, while all-sky searches scan for entirely unknown objects, which is crucial since most galactic neutron stars remain undiscovered.

Due to their large parameter spaces, fully-coherent all-sky searches are computationally prohibitive (Wette 2023) and hence semi-coherent methods (Tenorio et al. 2021) are usually employed. Semi-coherent methods split the data into shorter segments that are searched coherently and then incoherently combine together the results. Semi-coherent searches are less sensitive than coherent searches on the same data, but they can be tuned to be computationally feasible. Promising candidates from an initial semi-coherent search can then be further assessed with more sensitive semi-coherent searches having increasingly longer baseline segments.

The computational challenge increases when searching for unknown neutron stars in binary systems, as their orbital motion introduces additional parameters (Leaci & Prix 2015). For this reason only a relatively small subset of the possible signals from neutron stars in binaries have been explored. It is important to expand the searches for continuous wave emission from neutron stars in binaries because a large fraction of known millisecond pulsars are in binaries (Manchester et al. 2005), and because accretion may have generated the quadrupole moment (Rossetto et al. 2025; Hutchins & Jones 2023; Singh et al. 2020) required to make them detectable through their continuous gravitational-wave emission.

In this paper we present a search using the public O3 data from the Advanced LIGO detectors (Abbott et al. 2023). Our search covers signal frequencies up to 1000 Hz (see figure 1), almost doubling the maximum frequency previously investigated by a search of this kind. Allowing for the spin frequency of the objects to be high is important due to the recycling scenario, where neutron stars gain angular momentum due to the accretion of matter from their companion (Patruno & Watts 2020). Furthermore, some studies suggest that gravitational-wave emission could help to explain the observed spins of the galactic pulsar population (Gittins

& Andersson 2019), which is particularly important for neutron stars with high rotational frequencies like the ones targeted by this search.

## 2. THE SEARCH

### 2.1. Data

This search employs publicly available data from the third observing run (O3) (Abbott et al. 2023) of the Advanced LIGO Hanford (H1) and Advanced LIGO Livingston (L1) gravitational-wave detectors (Buikema et al. 2020). We use the GWOSC-16KHZ\_R1\_STRAIN channel and the DCS-CALIB\_STRAIN\_CLEAN\_SUB60HZ\_C01\_AR frame type, which is cleaned of non-Gaussian noise at the 60 Hz harmonics and calibration lines (Covas et al. 2018) prior to being publicly released. We further apply the gating procedure of Steltner et al. (2022) to remove short-duration glitches that increase the noise floor and reduce search sensitivity (e.g., Abbott et al. 2022).

From this data we produce short-baseline Fourier transforms (SFTs, see Allen & Mendell 2004) of 200 s (105 111 SFTs for H1 and 105 269 SFTs for L1), short enough to contain the signal power in a single frequency bin during this time. The amplitude spectral density (ASD)  $\sqrt{S_n}$  in the frequency range covered by this search is shown in figure 2.

### 2.2. Signal model and parameter space

We assume the CW signal model of Jaranowski et al. (1998).

This model depends on four amplitude parameters: the intrinsic gravitational-wave amplitude  $h_0$ , the angle between the angular momentum of the neutron star and the line of sight  $\iota$ , the polarization angle  $\psi$ , and the initial phase  $\phi_0$ . The model also depends on several phase-evolution parameters: the intrinsic gravitational-wave frequency  $f_0$  and its derivatives  $f_1, \dots, f_k$ , the sky position of the source  $\alpha, \delta$ , and the binary orbital parameters. The latter are the orbital period  $P_{\text{orb}}$ , the projected semi-major axis  $a_p$ , the time of ascension  $t_{\text{asc}}$ , the argument of periapsis  $\omega$ , and the eccentricity  $e$ , following the small-eccentricity model of Leaci & Prix (2015) that defines the orbit of the neutron star around the binary barycenter.

We search for signals across the entire sky, with gravitational-wave frequencies  $f_0$  indicated in table 1, covering over 86% of the known pulsars with orbital parameters in the examined ranges (Manchester et al. 2005).

We assume

$$|f_1| \leq \begin{cases} 4.67 \times 10^{-11} \text{ Hz/s} & \text{if } f_0 < 500 \text{ Hz,} \\ 6.61 \times 10^{-11} \text{ Hz/s} & \text{otherwise,} \end{cases} \quad (1)$$

which is consistent with the observed population of neutron stars in binaries (Manchester et al. 2005) and allows us to set  $f_1 = 0$  Hz/s for all templates in the initial stage of the search without increasing the mismatch by more than 2% with respect to templates with perfect match in signal spin-down.

The projected semi-major axis  $a_p$  of neutron stars in binary systems spans a broad range, determined by the companion mass  $M_C$ , orbital inclination  $\iota_b$ , and orbital period  $P_{\text{orb}}$ , as illustrated in figure 1. Due to the prohibitive computational cost of these searches, we select five different regions of the orbital parameter-space  $\{P_{\text{orb}}, a_p\}$  where neutron stars in binary systems lie (indicated by the black boxes in that figure and given in table 1). We also show the range of signal frequencies that we investigate, expressed in terms of the corresponding spin frequency  $\nu_0 = f_0/2$ . All our search regions contain unexplored areas, and region E was completely unexplored prior to this search (Aasi et al. 2014; Covas & Sintes 2020; Abbott et al. 2021; Covas et al. 2022, 2025; Abac et al. 2025).

Neutron stars in region E might be part of low mass X-ray binaries (LMXBs) with a less compact donor star. As shown in the right plot of figure 1, these neutron stars possess the highest rotational frequencies, which can be explained by the recycling scenario, where the neutron star accretes matter from its companion and gains angular momentum, a procedure which might provide the required asymmetry (Rossetto et al. 2025; Hutchins & Jones 2023; Singh et al. 2020). Furthermore, some studies suggest that long-lasting r-modes might be present in quiescent neutron stars in LMXBs, belonging to the so-called HOFNAR population (Chugunov et al. 2014). On the other hand, binary systems with a small orbital period are particularly difficult to search due to the increased template density (proportional to  $a_p^3/P_{\text{orb}}^5$ , see equation 77 of Leaci & Prix 2015) in that region.

We assume that the orbital eccentricity  $e$  is small:

$$e \leq \min(0.1, \hat{e}), \quad (2)$$

with

$$\hat{e} \equiv \begin{cases} 0.073 \left( \frac{200 \text{ Hz}}{f_0} \right) \left( \frac{P_{\text{orb}}}{10 \text{ days}} \right) \left( \frac{101\text{-s}}{a_p} \right) & \text{if } f_0 < 500 \text{ Hz,} \\ 0.026 \left( \frac{800 \text{ Hz}}{f_0} \right) \left( \frac{P_{\text{orb}}}{10 \text{ days}} \right) \left( \frac{101\text{-s}}{a_p} \right) & \text{otherwise.} \end{cases} \quad (3)$$

This allows us to set  $e = 0$  (and  $\omega = 0$ ) for all templates in the initial stage of the search while keeping the additional mismatch smaller than 2%. Only 9 out of 152 pulsars in binary systems located in these regions

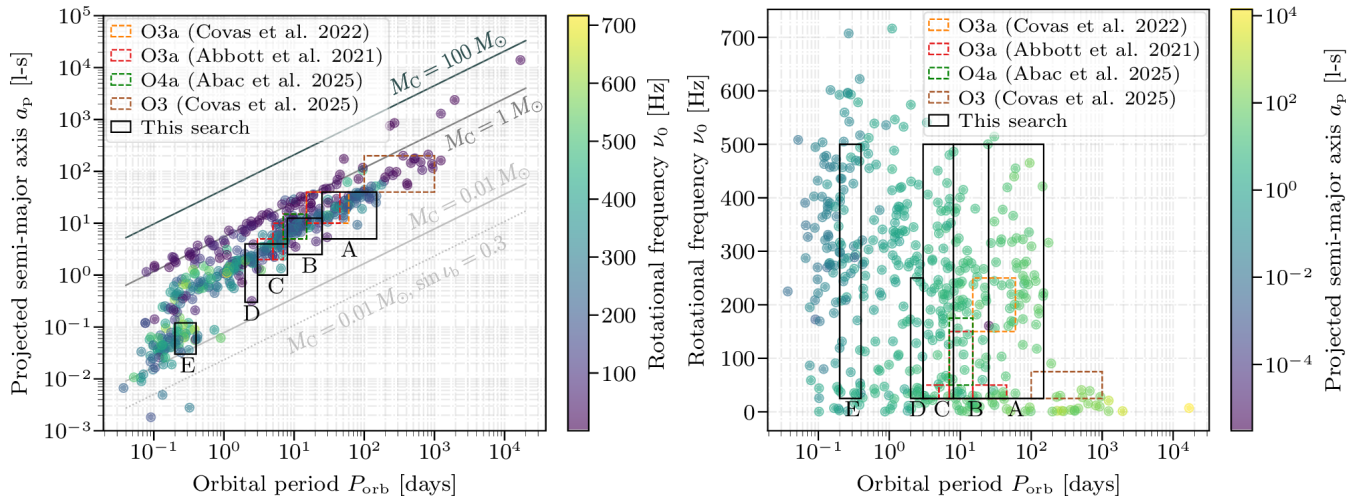


**Figure 1.** The black boxes show the signal-parameter regions covered by this search (left plot shows  $\{P_{\text{orb}}, a_p\}$ , right plot shows  $\{P_{\text{orb}}, \nu_0\}$ ). The circles show the known pulsars in binary systems from the ATNF catalog version 2.6.3 (Manchester et al. 2005) and the color encodes  $\nu_0$  (left plot) and  $a_p$  (right plot). The dashed boxes show the ranges covered by previous searches using O3 or O4 Advanced LIGO data. The different gray lines on the left plot show Kepler’s third law for different values of the companion mass  $M_C$  and inclination of the binary orbit  $\iota_b$  (continuous lines assume  $\iota_b = 90$  deg), assuming a neutron star mass of  $1.4 M_\odot$ .

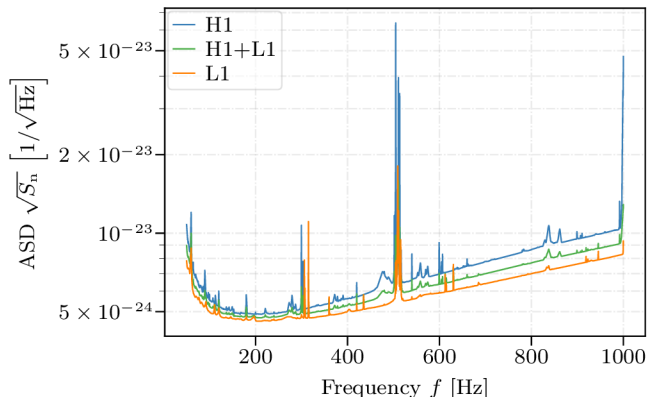


**Figure 2.** Square root of the harmonic mean power spectral density  $\sqrt{S_n}$  of the data used in this search as a function of frequency. The upper blue curve shows H1, the middle green curve shows H1+L1, and the lower orange curve shows L1.

(Manchester et al. 2005) have eccentricities outside of the range defined by equations (2) and (3).

### 2.3. Initial search

We use the BINARYSKYHOUF (Covas & Prix 2022a) semi-coherent search method with  $N_{\text{seg}} = 31675$  segments of length  $T_{\text{seg}} = 900$  s.

This search method uses templates with  $P_{\text{orb}} = 0$  at the coherent stage, and calculates the  $\mathcal{F}_{\text{AB};\ell}$  detection statistic of Covas & Prix (2022b) with  $\ell = 1, \dots, N_{\text{seg}}$  over a grid in  $f_0$  and sky.

We take a linear combination (with weights  $w_\ell$ ) of the  $\mathcal{F}_{\text{AB};\ell}$ , each tracking the time-frequency pattern pro-

duced by a possible signal, now including templates with non-zero values of  $\{P_{\text{orb}}, a_p, t_{\text{asc}}\}$ :

$$2\hat{\mathcal{F}}_{\text{AB}w} \equiv \sum_{\ell=1}^{N_{\text{seg}}} w_\ell 2\mathcal{F}_{\text{AB};\ell}. \quad (4)$$

The template grid spacings for the initial stage search are shown in table 2.

We exclude from the analysis the segments within the lowest 25th percentile of the  $w_\ell$ . This strategy results in a sensitivity loss smaller than  $\sim 5\%$ , while reducing the computational cost of the search by  $\sim 25\%$ .

We define a significance  $s$  for every template as

$$s \equiv \frac{2\hat{\mathcal{F}}_{\text{AB}w} - \mu}{\sigma}, \quad (5)$$

where  $\mu \equiv 2 \sum_\ell w_\ell = 2N_{\text{seg}}$  and  $\sigma^2 \equiv 4 \sum_\ell w_\ell^2$  are the expected mean and variance of  $2\hat{\mathcal{F}}_{\text{AB}w}$  in Gaussian noise. The significance  $s_i$  is our ranking statistic, where the index  $i$  indicates the stage of the search, with 0 being the initial stage.

More details about the set-up of the search are given in appendix A.

Figure 3 shows the most significant raw results of the search: in each of the five orbital parameter search regions we show the most significant (highest  $s_0$ ) result from every 0.1 Hz band. Prominent features below and above the average level can be attributed to different noise sources such as the 60 Hz power mains.

We use the clustering procedure of Covas & Sintes (2019, 2020) on initial stage results and group together

**Table 1.** Range of values for the different parameters covered by the search.  $t_m$  is the mid-time of the search, equal to 1 253 764 659.5 in GPS. A single value indicates an equal range for all orbital parameter-space regions.

Parameter	Region A	Region B	Region C	Region D	Region E
$f_0$ [Hz]	[50, 1000]	[50, 1000]	[50, 1000]	[50, 500]	[50, 1000]
$ f_1 $ [Hz/s]	see equation (1) and its discussion				
$\alpha$ [rad]	[0, $2\pi$ )				
$\delta$ [rad]	$[-\pi/2, \pi/2]$				
$a_p$ [l-s]	[5, 40]	[2.5, 12.5]	[1, 4]	[0.3, 4]	[0.03, 0.12]
$P_{\text{orb}}$ [days]	[25, 150]	[8, 25]	[3, 8]	[2, 3]	[0.2, 0.4]
$t_{\text{asc}}$ [GPS]	$[t_m - P_{\text{orb}}/2, t_m + P_{\text{orb}}/2]$				
$e$	see equation (2) and its discussion				
$\omega$ [rad]	[0, $2\pi$ )				

**Table 2.** Grid spacings of the initial stage of the search.  $\Omega = 2\pi/P_{\text{orb}}$  is the average angular orbital velocity.

Parameter	$f_0 < 500$ Hz	$f_0 \geq 500$ Hz
$\delta f_0$ [mHz]	1.1	1.1
$\delta\alpha$ [mrad]	$79.4 \left(\frac{200 \text{ Hz}}{f_0}\right)$	$27.8 \left(\frac{800 \text{ Hz}}{f_0}\right)$
$\delta\delta$ [mrad]	$79.4 \left(\frac{200 \text{ Hz}}{f_0}\right)$	$27.8 \left(\frac{800 \text{ Hz}}{f_0}\right)$
$\delta a_p$ [l-s]	$1.5 \left(\frac{200 \text{ Hz}}{f_0}\right) \left(\frac{P_{\text{orb}}}{10 \text{ days}}\right)$	$0.5 \left(\frac{800 \text{ Hz}}{f_0}\right) \left(\frac{P_{\text{orb}}}{10 \text{ days}}\right)$
$\delta\Omega$ [nHz]	$16.0 \left(\frac{200 \text{ Hz}}{f_0}\right) \left(\frac{P_{\text{orb}}}{10 \text{ days}}\right) \left(\frac{10 \text{ l-s}}{a_p}\right)$	$5.7 \left(\frac{800 \text{ Hz}}{f_0}\right) \left(\frac{P_{\text{orb}}}{10 \text{ days}}\right) \left(\frac{10 \text{ l-s}}{a_p}\right)$
$\delta t_{\text{asc}}$ [kGPS]	$20.1 \left(\frac{200 \text{ Hz}}{f_0}\right) \left(\frac{P_{\text{orb}}}{10 \text{ days}}\right)^2 \left(\frac{10 \text{ l-s}}{a_p}\right)$	$7.1 \left(\frac{800 \text{ Hz}}{f_0}\right) \left(\frac{P_{\text{orb}}}{10 \text{ days}}\right)^2 \left(\frac{10 \text{ l-s}}{a_p}\right)$

those likely caused by the same underlying source. The 3 clusters with the highest significance per 0.1 Hz band are saved for further analysis as candidates, yielding a total of 127 500 candidates: 28 500 candidates from the A, B, C, and E regions and 13 500 candidates from the D region of table 1.

#### 2.4. Follow-up

We follow-up these selected candidates by searching a volume of parameter space around each of them with a coherent time  $T_{\text{seg}} = 2700$  s, three times longer than that of the original search. On these reduced volumes we can leverage a nested sampling algorithm (Ashton et al. 2019) to calculate the detection statistic (Covas et al. 2024). We now explicitly search the  $f_1$ ,  $e$ , and  $\omega$  ranges given in table 1 due to the increased resolution.

To distinguish potential gravitational-wave signals from noise, we require the evolution of a candidate’s detection statistic to be consistent with the behavior of an astrophysical signal. This expected behavior is measured on simulated test-signals added to the O3 data (see appendix B for their distribution). In particular we consider two aspects: the consistent increase in significance  $s_1(s_0)$  and in the robust detection statistic  $\log_{10} \hat{B}_{1;\text{S/GLtL}}(s_0)$  (Keitel 2016) across stages 0 and 1. To calculate the  $\log_{10} \hat{B}_{1;\text{S/GLtL}}$  statistic we set the free parameter  $\hat{\mathcal{F}}^* = 0$ , which is equivalent to comparing a signal hypothesis with a single-detector line hypothesis, thus complementing the standard  $\mathcal{F}$ -statistic that compares signal and Gaussian noise hypotheses.

Figure 4 shows these quantities for both the simulated test-signals and the candidates. Based on the results from the simulated signals we define ac-

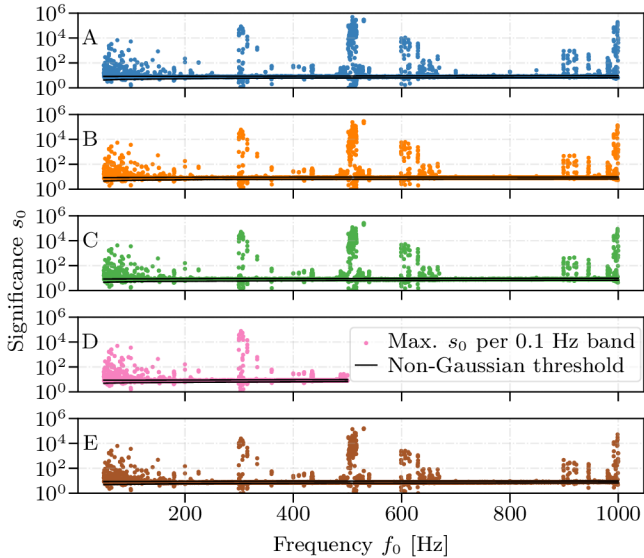


**Figure 3.** Maximum significance  $s_0$  of the initial stage in each 0.1 Hz frequency band as a function of the gravitational-wave frequency. The black lines show the threshold to consider a band non-Gaussian. A few bands with negative maximum  $s_0$  values are not shown on the plot.

ceptance/rejection regions in the  $s_0 - s_1$  and  $s_0 - \log_{10} \hat{B}_{1;S/GLtL}$  planes for the candidates. Our criteria has a false dismissal probability of about  $11/7200 \approx 0.15\%$  from 11 missed simulated signals and results in 15 candidates above both thresholds.

12 of these candidates can be associated with fake signals present in the data for validation purposes (the so-called “hardware injections”, see [Biwer et al. 2017](#)). The name “hardware injection” stems from these signals being produced by moving the detectors’ mirrors, rather than being added in software to the calibrated data. There are no hardware injection signals from the orbital parameter-space that we are investigating, but there are signals at the frequencies that we search from isolated neutron stars. Even though their waveforms do not match our binary ones, these signals are so loud, that our searches still identify them as unlikely to be due to noise. In particular 9 of our surviving candidates are related to the hardware injection at  $\sim 52.8$  Hz and 3 candidates to the one at  $\sim 848.9$  Hz. The other 3 surviving candidates (at 507.9 Hz, 517.2 Hz, and 998.3 Hz) can be associated with non-Gaussian disturbances, since they accumulate more than 80% of their signal-to-noise ratio from very few segments. We conclude that none of these candidates can be associated with a defensible CW signal.

### 3. ESTIMATED UPPER LIMITS

We estimate the 95% confidence upper limits on the gravitational-wave amplitude  $h_0^{95\%}$  in every 0.1 Hz band, which is the amplitude such that 95% of a population of signals with frequency in that band and with the same distribution for the other parameters as the simulated test-signals (see appendix B) would have been detected. The detection criterion for a simulated signal is that it generates a cluster with a higher significance than the 3rd cluster in its 0.1 Hz band and its orbital parameter-space region.

We can associate to each 0.1 Hz upper limit a corresponding sensitivity depth  $\mathcal{D}$  ([Behnke et al. 2015](#); [Dreisigacker et al. 2018](#)), which quantifies how far below the noise floor the smallest detectable signal lies, defined as

$$\mathcal{D}^{95\%} \equiv \frac{\sqrt{S_n}}{h_0^{95\%}}, \quad (6)$$

where  $\sqrt{S_n}$  is the harmonic mean amplitude spectral density of the data, shown in figure 2 with the middle green curve.

Due to the different grid spacings of the initial stage below and above 500 Hz (see appendix A for details), we determine the  $\langle \mathcal{D}_{\text{low}}^{95\%} \rangle$  and  $\langle \mathcal{D}_{\text{high}}^{95\%} \rangle$  of our search, separately for the low and high frequency range. The average is taken over the  $\mathcal{D}^{95\%}$  values obtained from the detection efficiency studies described above, across the different orbital parameter-space regions and the relevant frequency test-bands.

This yields  $\langle \mathcal{D}_{\text{low}}^{95\%} \rangle = 18.1 \pm 1.1 \text{ Hz}^{-1/2}$  and  $\langle \mathcal{D}_{\text{high}}^{95\%} \rangle = 17.1 \pm 0.9 \text{ Hz}^{-1/2}$ , with the second number indicating the standard deviation. We use these average sensitivity depths as a scale factor to determine the upper limits  $h_0^{95\%}$  in all frequency bands using equation (6).

The estimated upper limits are shown in the left plot of figure 5. The lowest upper limit is  $h_0^{95\%} = 2.63 \times 10^{-25}$  at  $f_0 = 211.1$  Hz. These results are available in machine-readable format at [Covas et al. \(2026\)](#).

Because the sensitivity depth is estimated based on detection efficiency studies carried out in noise not obviously affected by disturbances, upper limits estimates in disturbed bands are not trustworthy. We identify disturbed bands based on the expected value of the maximum significance  $s_0$ . When this exceeds the mean by 5 standard deviations, we assume that the band is disturbed and do not place an upper limit in it. Out of 9 500 0.1 Hz bands we identify 1 159 as disturbed. These bands are given in machine-readable format at [Covas et al. \(2026\)](#).

If the CWs are sourced by a mass asymmetry, the gravitational-wave amplitude is given by ([Bonazzola &](#)

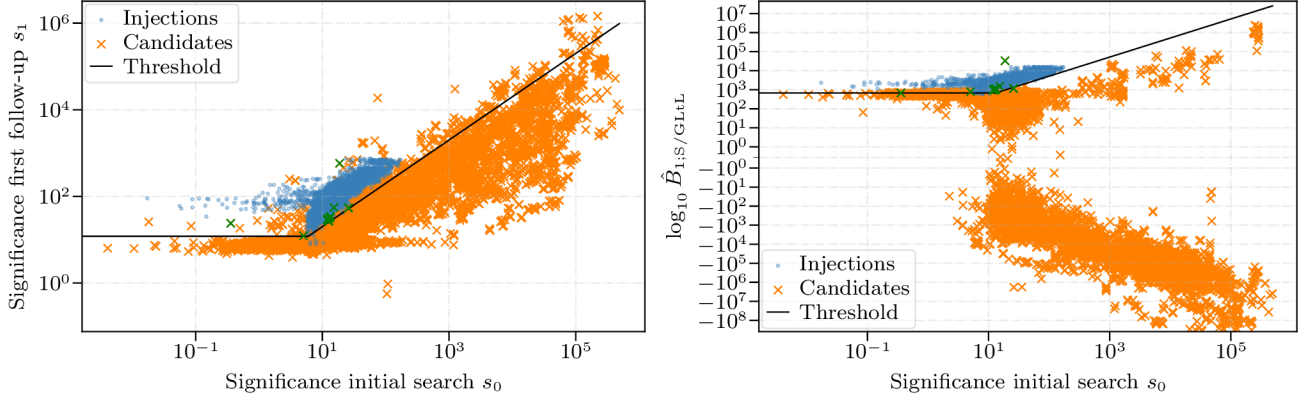


**Figure 4.** Distribution of significance values  $s_1$  (left plot) and  $\log_{10} \hat{B}_{1,S}/\text{GLTL}$  (right plot) for the follow-up. In the right plot we use a “symlog” scale, i.e., linear between -1 and 1. The blue circles show the 7200 simulated test-signals, and the crosses indicate the 127 500 search candidates, with the green crosses marking candidates that pass the vetoes. The region below the black line is the candidate-rejection region.

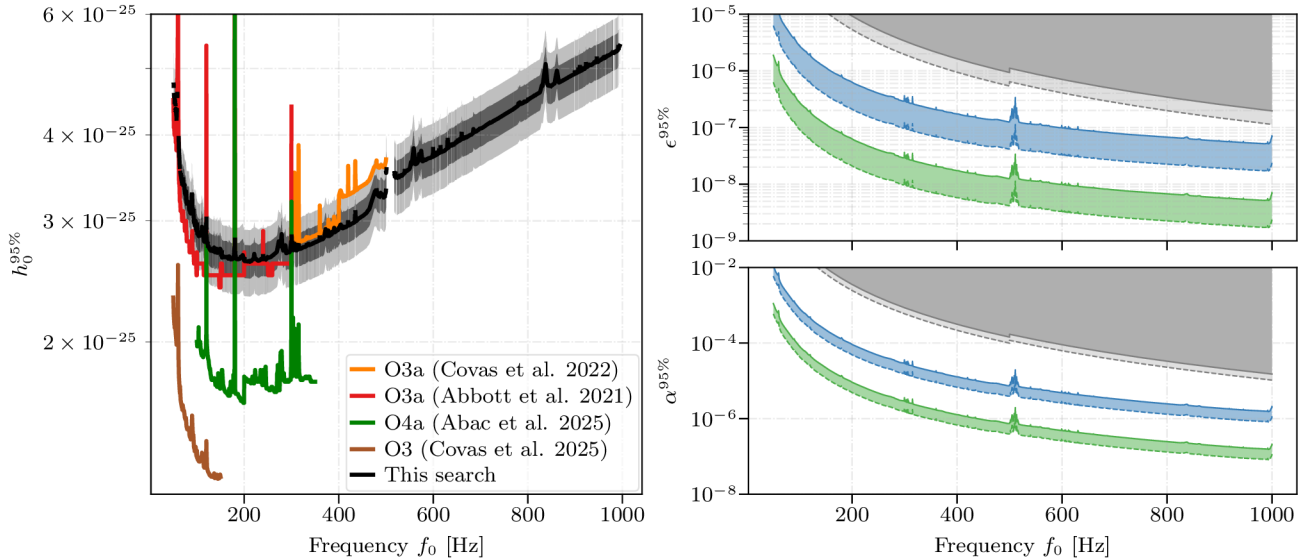


**Figure 5.** Estimated upper limits on the gravitational-wave amplitude  $h_0^{95\%}$  (left plot), on the neutron star ellipticity  $\epsilon$  (upper right plot), and on the r-mode amplitude  $\alpha$  (lower right plot) at the 95% confidence level as a function of the gravitational-wave frequency. Left plot: the black curve shows the results from this search, with the areas surrounding it indicating the  $1\sigma$  and  $2\sigma$  uncertainty regions. The other curves show the results from previous searches using O3 or O4 Advanced LIGO data. Right plots: the two different colors show results for distances of 100 pc (upper blue curves) and 10 pc (lower green curves). The upper shaded gray area shows the region where this search is not sensitive because the high ellipticities or r-mode amplitudes would generate a spin-down larger than the one probed by this search. In the upper right plot, the dashed lines assume  $I_{zz} = 3 \times 10^{38} \text{ kg m}^2$ , while the solid lines assume  $I_{zz} = 10^{38} \text{ kg m}^2$ . In the lower right plot, the dashed lines assume  $M = 1.9 M_\odot$  and  $R = 13 \text{ km}$ , while the solid lines assume  $M = 1.4 M_\odot$  and  $R = 11.7 \text{ km}$ .

Gourgoulhon 1996)

$$h_0 \simeq 10^{-26} \left( \frac{\epsilon}{10^{-6}} \right) \left( \frac{I_{zz}}{10^{38} \text{ kg m}^2} \right) \times \left( \frac{f_0}{100 \text{ Hz}} \right)^2 \left( \frac{1 \text{ kpc}}{d} \right), \quad (7)$$

where  $\epsilon = |I_{xx} - I_{yy}|/I_{zz}$  is the equatorial ellipticity,  $I_{zz}$  is the moment of inertia of the star with respect to

the principal axis aligned with the rotational axis, and  $d$  is the distance. On the other hand, if the CWs are sourced by r-modes, the gravitational-wave amplitude

is given by (Owen 2010)

$$h_0 \simeq 10^{-26} \left( \frac{\alpha}{2.8 \times 10^{-4}} \right) \left( \frac{M}{1.4 M_\odot} \right) \left( \frac{R}{11.7 \text{ km}} \right)^3 \times \left( \frac{f_0}{100 \text{ Hz}} \right)^3 \left( \frac{1 \text{ kpc}}{d} \right), \quad (8)$$

where  $\alpha$  is the r-mode amplitude,  $M$  is the mass of the neutron star, and  $R$  its radius.

The estimated upper limits on  $h_0$  can hence be used to constrain the equatorial ellipticity and the r-mode amplitude of the targeted neutron star population by rearranging equations (7) and (8). The ellipticity upper limits depend on the value for the moment of inertia of the neutron star, which is uncertain by around a factor of three (see section 4B of Abbott et al. 2007 and figure 4 of Fantina et al. 2022), although more exotic neutron star models such as quark stars, and lower-mass or larger-radius neutron stars could yield higher moments of inertia (Horowitz 2010; Owen 2005). The r-mode amplitude upper limits depend on the neutron star mass and radius which are related by the neutron star equation of state.

The upper right plot of figure 5 shows the ellipticity upper limits for two distances and two values of the moment of inertia. The tightest constraint for the ellipticity is achieved at  $f_0 = 989.9 \text{ Hz}$ , which for sources at 100 pc with  $I_{zz} = 10^{38} \text{ kg m}^2$  is  $\epsilon < 5.2 \times 10^{-8}$ . If instead we assume  $I_{zz} = 3 \times 10^{38} \text{ kg m}^2$ , the upper limits are more stringent, as shown by the dashed traces. For example, for sources within 100 pc at 989.9 Hz, we find  $\epsilon < 1.7 \times 10^{-8}$ , which is well within the predicted maximum ellipticities of neutron stars, that range between  $10^{-8}$  and  $10^{-5}$  (Rossetto et al. 2025; Gittins & Andersson 2021).

The lower right plot of figure 5 shows the r-mode amplitude upper limits for two different distances and two mass-radius combinations. The tightest constraint for the r-mode amplitude is achieved at  $f_0 = 993.3 \text{ Hz}$ , which for sources at 100 pc with  $M = 1.4 M_\odot$  and  $R = 11.7 \text{ km}$  is  $\alpha < 1.5 \times 10^{-6}$ . If instead we assume  $M = 1.9 M_\odot$  and  $R = 13 \text{ km}$ , our constraint becomes more stringent:  $\alpha < 8.1 \times 10^{-7}$ . Theoretical predictions on r-mode amplitudes are  $\alpha \sim 8 \times 10^{-7} - 10^{-4}$  (Gusakov et al. 2014a,b) or  $\alpha \sim 10^{-5}$  (Bondarescu et al. 2007), which are by and large within the range that we have probed.

#### 4. CONCLUSIONS

In this paper we present the most extensive search to date for CWs from unknown neutron stars in binary systems, with gravitational-wave frequencies between 50 and 1000 Hz and orbital periods between 0.2

and 150 days. The main objective of this search is to cover the widest possible parameter-space region with a certain computational budget. For this reason we use coarser template grids and a shorter coherent time-baseline compared to our other recent search (Covas et al. 2025), whose main objective was to achieve the best possible sensitivity.

We use the BINARYSKYHOU $\mathcal{F}$  pipeline, which is the most efficient and sensitive pipeline to carry out this type of search. We do not detect any astrophysical signal. The main search has taken  $\sim 10.15 \times 10^6$  CPU core-hours to complete, running on a combination of AMD EPYC 7402 CPUs and NVIDIA A100 GPUs. The computational cost of the follow-up is negligible.

Previous searches such as Abbott et al. (2021); Abac et al. (2025) are  $\approx 20\%$  more sensitive than this search but cover a much smaller parameter-space. Specifically this search reaches frequencies  $\sim 3$  times larger, which is particularly difficult because the computational cost scales  $\propto f_0^5$ . Additionally this search covers large regions of the orbital parameter-space, some of which have not been searched before. Using the ‘‘breadth’’  $\mathcal{B}$  to quantify the extent of the investigated parameter space, from equation (75) of Wette (2023), we find that our parameter space is about 4 orders of magnitude larger than ever investigated with Advanced LIGO data.

As the plots of figure 1 show, vast regions of parameter space remain unexplored. This search demonstrates what state-of-the art search techniques can achieve in the challenging high-frequency range and may be used as blueprint for investigating new and more sensitive datasets.

#### ACKNOWLEDGMENTS

We acknowledge the contribution of Benjamin Steltner who prepared the SFT data for this search.

This project has received funding from the European Union’s Horizon 2020 research and innovation program under the Marie Skłodowska-Curie Grant Agreement No. 101029058.

This work was supported by the Universitat de les Illes Balears (UIB) with funds from the Programa de Foment de la Recerca i la Innovació de la UIB 2024-2026 (supported by the yearly plan of the Tourist Stay Tax ITS2023-086); the Spanish Agencia Estatal de Investigación (AEI) grants PID2024-157460NA-100, RED2024-153978-E, RED2024-153735-E, funded by MICIU/AEI/10.13039/501100011033 and the ERDF/EU; and the Comunitat Autònoma de les Illes Balears through the Conselleria d’Educació i Universitats with funds from the European Union - European Re-

gional Development Fund (ERDF) (SINCO2022/18146 - Plataforma HiTech-IAC3-BIO).

We acknowledge PRACE for awarding us access to JUWELS Booster at GCS@JSC, Germany.

This work has utilized the ATLAS cluster computing at MPI for Gravitational Physics Hannover and the

HPC system Raven at the Max Planck Computing and Data Facility.

This research has made use of data or software obtained from the Gravitational Wave Open Science Center (gwosc.org), a service of the LIGO Scientific Collaboration, the Virgo Collaboration, and KAGRA (Abbott et al. 2023).

## APPENDIX

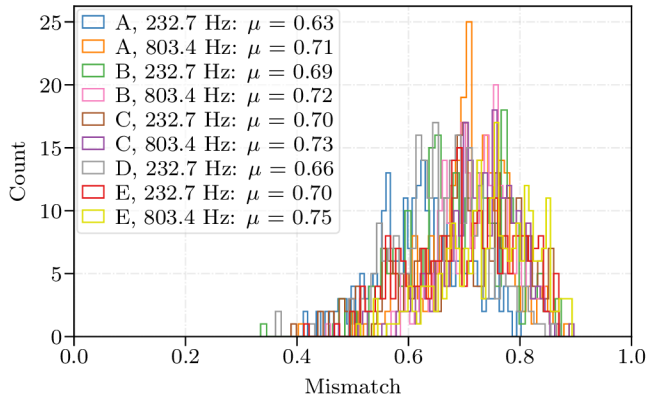


**Figure 6.** Mismatch distribution of this search at two different frequencies, in the 200 Hz and 800 Hz region, respectively. The other parameters that describe the CW signal span the ranges given in table 1. The legend shows the mean of each distribution for each different region of orbital parameter-space.

### A. INITIAL STAGE SET-UP DETAILS

The mismatch distributions for the various orbital parameter regions at two representative frequencies are shown in figure 6. The number of waveforms searched in each 0.1 Hz frequency band is shown in figure 7.

### B. DISTRIBUTION OF SIMULATED TEST-SIGNALS AND UPPER LIMITS

The parameters of the simulated signals that we use to calibrate the follow-up procedure and to estimate the upper limits are drawn from the search ranges given in table 1. The sky position of the signals is drawn from a distribution isotropic on the celestial sphere. The frequency  $f_0$  is drawn uniformly from 0.1 Hz test-bands. The noise in these test-bands is representative of the vast majority of the frequency ranges in our data, and is not affected by disturbances. We use 10 different bands below 500 Hz and 10 bands above 500 Hz. Spin-down  $f_1$  and eccentricity  $e$  are log-uniformly distributed. The smallest spin-down and eccentricity values are taken two orders of magnitude below the maximum values.

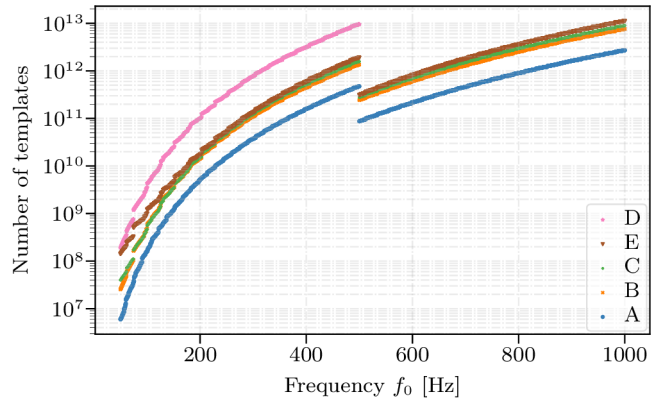


**Figure 7.** Number of templates searched in a 0.1 Hz frequency band as a function of the gravitational-wave frequency. The different colors show the different regions of orbital parameter-space. The total number of templates is  $\sim 6.3 \times 10^{16}$ .

The amplitudes  $h_0$  are chosen by uniformly sampling the sensitivity depth (see equation (6)) from the range  $[12, 49.5] \text{ Hz}^{-1/2}$  (in discrete steps of  $2.5 \text{ Hz}^{-1/2}$ ). The other amplitude parameters  $\cos \iota$ ,  $\psi$ , and  $\phi_0$  are uniformly distributed.

We use 32 000 signals for each orbital region (16 000 for region D), with 100 signals per frequency band and sensitivity depth value. To determine the follow-up thresholds shown in figure 4, we use a subset of test-signals detected by the initial stage, i.e., 7 200 signals corresponding to 10 signals for each frequency band and sensitivity depth value, and only using 5 of the 10 frequency bands below 500 Hz and 5 of the 10 bands above 500 Hz. We do this to limit the computational cost of these tuning studies.

To estimate the upper limits we compute the fraction of detected signals as a function of the sensitivity depth  $\mathcal{D}$  of the signals, a standard procedure also employed by several other searches (Abbott et al. 2021; Covas & Sintes 2020; Steltner et al. 2021). We determine the sensitivity depth necessary to achieve 95% detection efficiency for each frequency band and orbital

region combination. We do this by using an interpolation, as exemplified by figure 8. We finally average the 95% confidence sensitivity depth values from the low-frequency bands and from the high-frequency bands, yielding  $\langle \mathcal{D}_{\text{low}}^{95\%} \rangle = 18.1 \text{ Hz}^{-1/2}$  and  $\langle \mathcal{D}_{\text{high}}^{95\%} \rangle = 17.1 \text{ Hz}^{-1/2}$ , respectively.

We have only tested the sensitivity of our search with signals distributed in the ranges given in table 1. If a putative signal lies outside these ranges, then the false-dismissal probability that we have estimated would be increased. Quantifying this is outside of the scope of this paper.

The signal model described in section 2.2 and commonly used in CW searches assumes phase coherence for the duration of each coherent segment. While this model is a very reasonable assumption for fast spinning neutron stars, it is known that some pulsars exhibit glitches (Ashton et al. 2017), spin-wandering (Mukherjee et al. 2018), and timing noise (Ashton et al. 2015). A loss of phase coherence will impact the sensitivity of a search if it is resolvable by it. We refer the reader to the detailed discussion of section 4.2 in Covas et al. (2025) regarding the robustness of our results to deviations from the

assumed CW signal model. We remark that the longest coherent time that we have used in this search is only 2700 s, shorter than the one used in that search, making these results more robust to deviations of the signal from the assumed model.

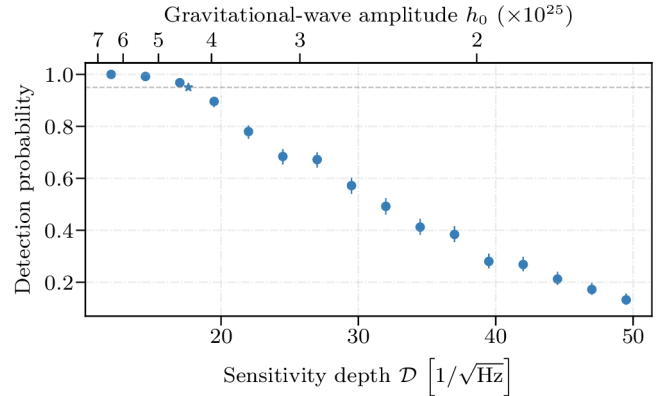


**Figure 8.** Illustrative example of the detection probability as a function of the normalized inverse signal-amplitude ( $\mathcal{D}$ ) for signals at  $\approx 803.4 \text{ Hz}$  and with orbital parameters from region A. The top axis shows the corresponding values of the signal amplitude ( $h_0$ ). The error bars show the  $1\sigma$  uncertainty, and the star marker shows the interpolated value of  $\mathcal{D}^{95\%}$ .

## REFERENCES

- Aasi, J., Abbott, B. P., Abbott, R., et al. 2014, *Phys. Rev. D*, 90, 062010, doi: [10.1103/PhysRevD.90.062010](https://doi.org/10.1103/PhysRevD.90.062010)
- Abac, A. G., Abouelfettouh, I., Acernese, F., et al. 2025, arXiv, 2511.16863, doi: [10.48550/arXiv.2511.16863](https://doi.org/10.48550/arXiv.2511.16863)
- Abbott, B., Abbott, R., Adhikari, R., et al. 2007, *Phys. Rev. D*, 76, 042001, doi: [10.1103/PhysRevD.76.042001](https://doi.org/10.1103/PhysRevD.76.042001)
- Abbott, R., Abbott, T. D., Abraham, S., et al. 2021, *Phys. Rev. D*, 103, 064017, doi: [10.1103/PhysRevD.103.064017](https://doi.org/10.1103/PhysRevD.103.064017)
- Abbott, R., Abe, H., Acernese, F., et al. 2022, *Phys. Rev. D*, 106, 102008, doi: [10.1103/PhysRevD.106.102008](https://doi.org/10.1103/PhysRevD.106.102008)
- . 2023, *Astrophys. J. Supplement Series*, 267, 29, doi: [10.3847/1538-4365/acdc9f](https://doi.org/10.3847/1538-4365/acdc9f)
- Allen, B., & Mendell, G. 2004, Tech. Rep. T040164. <https://dcc.ligo.org/LIGO-T040164/public>
- Ashton, G., Jones, D. I., & Prix, R. 2015, *Phys. Rev. D*, 91, 062009, doi: [10.1103/PhysRevD.91.062009](https://doi.org/10.1103/PhysRevD.91.062009)
- Ashton, G., Prix, R., & Jones, D. I. 2017, *Phys. Rev. D*, 96, 063004, doi: [10.1103/PhysRevD.96.063004](https://doi.org/10.1103/PhysRevD.96.063004)
- Ashton, G., Hübner, M., Lasky, P. D., et al. 2019, *Astrophys. J. Supplement Series*, 241, 27, doi: [10.3847/1538-4365/ab06fc](https://doi.org/10.3847/1538-4365/ab06fc)
- Behnke, B., Papa, M. A., & Prix, R. 2015, *Phys. Rev. D*, 91, 064007, doi: [10.1103/PhysRevD.91.064007](https://doi.org/10.1103/PhysRevD.91.064007)
- Biwer, C., Barker, D., Batch, J. C., et al. 2017, *Phys. Rev. D*, 95, 062002, doi: [10.1103/PhysRevD.95.062002](https://doi.org/10.1103/PhysRevD.95.062002)
- Bonazzola, S., & Gourgoulhon, E. 1996, *A&A*, 312, 675, doi: [10.48550/arXiv.astro-ph/9602107](https://doi.org/10.48550/arXiv.astro-ph/9602107)
- Bondarescu, R., Teukolsky, S. A., & Wasserman, I. 2007, *Phys. Rev. D*, 76, 064019, doi: [10.1103/PhysRevD.76.064019](https://doi.org/10.1103/PhysRevD.76.064019)
- Buikema, A., Cahillane, C., Mansell, G. L., et al. 2020, *Phys. Rev. D*, 102, 062003, doi: [10.1103/PhysRevD.102.062003](https://doi.org/10.1103/PhysRevD.102.062003)
- Chugunov, A. I., Gusakov, M. E., & Kantor, E. M. 2014, *MNRAS*, 445, 385, doi: [10.1093/mnras/stu1772](https://doi.org/10.1093/mnras/stu1772)
- Covas, P. B., Papa, M. A., & Prix, R. 2025, *Astrophys. J.*, 985, 192, doi: [10.3847/1538-4357/adcc2b](https://doi.org/10.3847/1538-4357/adcc2b)
- . 2026, <https://www.aei.mpg.de/continuouswaves/O3AllSkyBinary2>
- Covas, P. B., Papa, M. A., Prix, R., & Owen, B. J. 2022, *Astrophys. J. Lett.*, 929, L19, doi: [10.3847/2041-8213/ac62d7](https://doi.org/10.3847/2041-8213/ac62d7)
- Covas, P. B., & Prix, R. 2022a, *Phys. Rev. D*, 106, 084035, doi: [10.1103/PhysRevD.106.084035](https://doi.org/10.1103/PhysRevD.106.084035)
- . 2022b, *Phys. Rev. D*, 105, 124007, doi: [10.1103/PhysRevD.105.124007](https://doi.org/10.1103/PhysRevD.105.124007)

- Covas, P. B., Prix, R., & Martins, J. 2024, *Phys. Rev. D*, 110, 024053, doi: [10.1103/PhysRevD.110.024053](https://doi.org/10.1103/PhysRevD.110.024053)
- Covas, P. B., & Sintes, A. 2020, *Phys. Rev. Lett.*, 124, 191102, doi: [10.1103/PhysRevLett.124.191102](https://doi.org/10.1103/PhysRevLett.124.191102)
- Covas, P. B., & Sintes, A. M. 2019, *Phys. Rev. D*, 99, 124019, doi: [10.1103/PhysRevD.99.124019](https://doi.org/10.1103/PhysRevD.99.124019)
- Covas, P. B., Effler, A., Goetz, E., et al. 2018, *Phys. Rev. D*, 97, 082002, doi: [10.1103/PhysRevD.97.082002](https://doi.org/10.1103/PhysRevD.97.082002)
- Dreissigacker, C., Prix, R., & Wette, K. 2018, *Phys. Rev. D*, 98, 084058, doi: [10.1103/PhysRevD.98.084058](https://doi.org/10.1103/PhysRevD.98.084058)
- Fantina, A. F., Zdunik, J. L., Chamel, N., et al. 2022, *A&A*, 665, A74, doi: [10.1051/0004-6361/202243715](https://doi.org/10.1051/0004-6361/202243715)
- Gittins, F., & Andersson, N. 2019, *MNRAS*, 488, 99–110, doi: [10.1093/mnras/stz1719](https://doi.org/10.1093/mnras/stz1719)
- . 2021, *MNRAS*, 507, 116, doi: [10.1093/mnras/stab2048](https://doi.org/10.1093/mnras/stab2048)
- Gusakov, M. E., Chugunov, A. I., & Kantor, E. M. 2014a, *Phys. Rev. Lett.*, 112, 151101, doi: [10.1103/PhysRevLett.112.151101](https://doi.org/10.1103/PhysRevLett.112.151101)
- . 2014b, *Phys. Rev. D*, 90, 063001, doi: [10.1103/PhysRevD.90.063001](https://doi.org/10.1103/PhysRevD.90.063001)
- Horowitz, C. J. 2010, *Phys. Rev. D*, 81, 103001, doi: [10.1103/PhysRevD.81.103001](https://doi.org/10.1103/PhysRevD.81.103001)
- Hutchins, T. J., & Jones, D. I. 2023, *MNRAS*, 522, 226, doi: [10.1093/mnras/stad967](https://doi.org/10.1093/mnras/stad967)
- Jaranowski, P., Królak, A., & Schutz, B. F. 1998, *Phys. Rev. D*, 58, 063001, doi: [10.1103/PhysRevD.58.063001](https://doi.org/10.1103/PhysRevD.58.063001)
- Jones, D. I., & Riles, K. 2025, *Class. Quant. Grav.*, 42, 033001, doi: [10.1088/1361-6382/ada244](https://doi.org/10.1088/1361-6382/ada244)
- Keitel, D. 2016, *Phys. Rev. D*, 93, 084024, doi: [10.1103/PhysRevD.93.084024](https://doi.org/10.1103/PhysRevD.93.084024)
- Leaci, P., & Prix, R. 2015, *Phys. Rev. D*, 91, 102003, doi: [10.1103/PhysRevD.91.102003](https://doi.org/10.1103/PhysRevD.91.102003)
- Manchester, R. N., Hobbs, G. B., Teoh, A., & Hobbs, M. 2005, *Astronom. J.*, 129, 1993–2006, doi: [10.1086/428488](https://doi.org/10.1086/428488)
- Mukherjee, A., Messenger, C., & Riles, K. 2018, *Phys. Rev. D*, 97, 043016, doi: [10.1103/PhysRevD.97.043016](https://doi.org/10.1103/PhysRevD.97.043016)
- Owen, B. J. 2005, *Phys. Rev. Lett.*, 95, 211101, doi: [10.1103/PhysRevLett.95.211101](https://doi.org/10.1103/PhysRevLett.95.211101)
- . 2010, *Phys. Rev. D*, 82, 104002, doi: [10.1103/PhysRevD.82.104002](https://doi.org/10.1103/PhysRevD.82.104002)
- Patruno, A., & Watts, A. L. 2020, *Accreting Millisecond X-ray Pulsars* (Springer Berlin Heidelberg), 143–208, doi: [10.1007/978-3-662-62110-3\\_4](https://doi.org/10.1007/978-3-662-62110-3_4)
- Riles, K. 2023, *Liv. Rev. in Relat.*, 26, 1, doi: [10.1007/s41114-023-00044-3](https://doi.org/10.1007/s41114-023-00044-3)
- Rossetto, P. H. B., Frauendiener, J., & Melatos, A. 2025, *Astrophys. J.*, 979, 10, doi: [10.3847/1538-4357/ada276](https://doi.org/10.3847/1538-4357/ada276)
- Singh, N., Haskell, B., Mukherjee, D., & Bulik, T. 2020, *MNRAS*, 493, 3866, doi: [10.1093/mnras/staa442](https://doi.org/10.1093/mnras/staa442)
- Steltner, B., Papa, M., & Eggenstein, H. 2022, *Phys. Rev. D*, 105, 022005, doi: [10.1103/PhysRevD.105.022005](https://doi.org/10.1103/PhysRevD.105.022005)
- Steltner, B., Papa, M. A., Eggenstein, H.-B., et al. 2021, *Astrophys. J.*, 909, 79, doi: [10.3847/1538-4357/abc7c9](https://doi.org/10.3847/1538-4357/abc7c9)
- Tenorio, R., Keitel, D., & Sintes, A. M. 2021, *Universe*, 7, 474, doi: [10.3390/universe7120474](https://doi.org/10.3390/universe7120474)
- Wette, K. 2023, *Astroparticle Physics*, 153, 102880, doi: [10.1016/j.astropartphys.2023.102880](https://doi.org/10.1016/j.astropartphys.2023.102880)